Research Article | Vol. 26, No. 1 | 8 Jan 2018 | OPTICS EXPRESS 402
Optics EXPRESS

Planar polarization-routing optical cross-connects using nematic liquid crystal waveguides

TENGHAO LI,[1,2] QINGMING CHEN,[1,2] WEIXING YU,[3] AND XUMING ZHANG[1,2,*]

[1]*Department of Applied Physics, The Hong Kong Polytechnic University, Hong Kong, China*
[2]*The Hong Kong Polytechnic University Shenzhen Research Institute, Shenzhen, 518057, China*
[3]*Key Laboratory of Spectral Imaging Technology, Xi'an Institute of Optics and Precision Mechanics, Chinese Academy of Sciences, Xi'an, Shaanxi, 710119, China*
*apzhang@polyu.edu.hk

Abstract: This paper presents the device design and performance analysis of a novel design of planar optical cross-connect (OXC) using nematic liquid crystal (NLC) waveguides. It employs N × N switching matrix in cross-bar fabric. In each unit cell, the input light is set in either the transverse electric (TE) mode or the transverse magnetic (TM) mode by electrically reorienting the NLC in the waveguide. The light then enters a passive waveguide and is routed to different paths depending on the polarization state (TE/TM mode). A sample device of 8 × 8 OXC is analyzed for performance estimation, which predicts a maximum on-chip insertion loss of 3 dB, an average cross-talk of –40 dB, ~1 ms switching time, and 2 mm × 2 mm footprint. The proposed OXC is unique in the switching mechanism of polarization-dependent routing and allows non-blocking switching with high compactness and broad bandwidth. It is potential for optical circuit switching in data centers and optical communication networks.

OCIS codes: (230.3720) Liquid-crystal devices; (060.0060) Fiber optics and optical communications; (060.1810) Buffers, couplers, routers, switches, and multiplexers; (130.4815) Optical switching devices.

References and links

1. T. S. El-Bawab, *Optical Switching* (Springer Press, 2006), pp. 1–32.
2. C. Kachris, K. Kanonakis, and I. Tomkos, "Optical interconnection networks in data centers: recent rrends and future challenges," IEEE Commun. Mag. **51**(9), 39–45 (2013).
3. G. Wang, D. G. Andersen, M. Kaminsky, T. S. E. Ng, K. Papagiannaki, M. Glick, and L. Mummert, "Your data center is a router: the case for reconfigurable optical circuit switched paths," in 2009 ACM HotNets-VIII, 1–6.
4. K. Chen, A. Singla, A. Singh, K. Ramachandran, L. Xu, Y. Zhang, X. Wen, and Y. Chen, "OSA: an optical switching architecture for data center networks with unprecedented flexibility," IEEE/ACM Trans. Netw. **22**(2), 498–511 (2014).
5. J. Kim, C. J. Nuzman, B. Kumar, D. F. Lieuwen, J. S. Kraus, A. Weiss, C. P. Lichtenwalner, A. R. Papazian, R. E. Frahm, N. R. Basavanhally, D. A. Ramsey, V. A. Aksyuk, F. Pardo, M. E. Simon, V. Lifton, H. B. Chan, M. Haueis, A. Gasparyan, H. R. Shea, S. Arney, C. A. Bolle, P. R. Kolodner, R. Ryf, D. T. Neilson, and J. V. Gates, "1100 x 1100 port MEMS-based optical crossconnect with 4-dB maximum loss," IEEE Photonics Technol. Lett. **15**(11), 1537–1539 (2003).
6. R. Stabile, A. Albores-Mejia, A. Rohit, and K. A. Williams, "Integrated optical switch matrices for packet data networks," Microsystems & Nanoengineering **2**, 15042 (2016).
7. L. Chen and Y. K. Chen, "Compact, low-loss and low-power 8×8 broadband silicon optical switch," Opt. Express **20**(17), 18977–18985 (2012).
8. R. Ji, L. Yang, L. Zhang, Y. Tian, J. Ding, H. Chen, Y. Lu, P. Zhou, and W. Zhu, "Five-port optical router for photonic networks-on-chip," Opt. Express **19**(21), 20258–20268 (2011).
9. Q. Cheng, M. Ding, A. Wonfor, and I. H. White, "The feasibility of building a 64 x 64 port count SOA-based optical switch," in 2015 International Conference on Photonics in Switching (PS2015), pp. 199–201.
10. S. Han, T. Seok, N. Quack, B. Yoo, and M. Wu, "Large-scale silicon photonic switches with movable directional couplers," Optica **2**(4), 370–375 (2015).
11. T. J. Seok, N. Quack, S. Han, R. S. Muller, and M. C. Wu, "Large-scale broadband digital silicon photonic switches with vertical adiabatic couplers," Optica **3**(1), 64–70 (2016).
12. H. Du, F. Chau, and G. Zhou, "Mechanically-tunable photonic devices with on-chip integrated MEMS/NEMS actuators," Micromachines (Basel) **7**(4), 69 (2016).

#313781 https://doi.org/10.1364/OE.26.000402
Journal © 2018 Received 20 Nov 2017; revised 17 Dec 2017; accepted 20 Dec 2017; published 4 Jan 2018

Optics EXPRESS

13. D. K. Yang and S. T. Wu, *Fundmentals of Liquid Crystal Devices* (John Wiley & Sons, 2015), pp. 1–285.
14. Z. Zhuang, Y. J. Kim, and J. S. Patel, "Achromatic linear polarization rotator using twisted nematic liquid crystals," Appl. Phys. Lett. **76**(26), 3995–3997 (2000).
15. P. Fiala, C. Dorrer, and K. Marshall, "Twisted-nematic liquid crystal polarization rotators for broadband laser applications," in CLEO: 2015, OSA Technical Digest (online) (Optical Society of America, 2015), paper JW2A.68.
16. Q. Wang and G. Farrell, "Integrated liquid-crystal switch for both TE and TM modes: proposal and design," J. Opt. Soc. Am. A **24**(10), 3303–3308 (2007).
17. G. Chen and J. U. Kang, "Waveguide mode converter based on two-dimensional photonic crystals," Opt. Lett. **30**(13), 1656–1658 (2005).
18. P. Wang, G. Brambilla, Y. Semenova, Q. Wu, J. Zheng, and G. Farrell, "Proposal for a simple polarization converter based on integrated optical ion exchanged waveguide," Optical Communications and Networks (ICOCN 2010), 9th International Conference on, Nanjing, 2010, 441–444.
19. Q. Gong, S. Gong, H. Zhang, L. Liu, and Y. Wang, "Synthesis of a novel polyimide used as liquid crystal vertical alignment layers," RSC Advances **5**(70), 57245–57253 (2015).
20. W. J. Zheng and M. H. Huang, "Use of polydimethylsiloxane thin film as vertical liquid crystal alignment layer," Thin Solid Films **520**(7), 2841–2845 (2012).
21. P. J. Hamelinck and W. T. S. Huck, "Homeotropic alignment on surface-initiated liquid crystalline polymer brushes," J. Mater. Chem. **15**(3), 381–385 (2005).
22. Norland Products, Inc., Norland Optical Adhesive 84, Available at https://www.norlandprod.com/adhesives/noa%2084.html.
23. T. D. Flaim, Y. Wang, and R. Mercado, "High refractive index polymer coatings for optoelectronic applications," Proc. SPIE **5250**, 423–434 (2004).
24. R. Jones, O. Cohen, H. Chan, D. Rubin, A. Fang, and M. Paniccia, "Integration of SiON gratings with SOI," IEEE International Conference on Group IV Photonics, **2005**, 192–194 (2005).
25. A. V. Zakharov and R. Y. Dong, "Dielectric and elastic properties of liquid crystals," Phys. Rev. E Stat. Nonlin. Soft Matter Phys. **64**(3 Pt 1), 031701 (2001).
26. J. Li and S. T. Wu, "Extended Cauchy equations for the refractive indices of liquid crystals," J. Appl. Phys. **95**(3), 896–901 (2004).
27. D. Hermann, Integrated Optics with Liquid Crystals, Available at http://fy.chalmers.se/-f9adh/pub/LCIO-Hermann.pdf, Chalmers Univ. of Tech., Goteberg, SE, (2000), 1–33.
28. S. Ertman, T. R. Wolinski, D. Pysz, R. Buczynski, E. Nowinowski-Kruszelnicki, and R. Dabrowski, "Low-loss propagation and continuously tunable birefringence in high-index photonic crystal fibers filled with nematic liquid crystals," Opt. Express **17**(21), 19298–19310 (2009).
29. E. D. Palik, *Handbook of Optical Constants of Solids* (Academic Press, 1985).
30. Norland Products, Inc., Norland Optical Adhesive 61, Available at https://www.norlandprod.com/adhesives/noa%2061.html.
31. L. Colombo, J. J. Chamber, and H. Niimi, "Gate dielectric process technology for the sub-1 nm equivalent oxide thickness (EOT) era," Electrochem. Soc. Interface **16**(3), 51–55 (2007).
32. Y. Fu, T. Ye, W. Tang, and T. Chu, "Efficient adiabatic silicon-on-insulator waveguide taper," Photon. Res. **2**(3), A41–A44 (2014).
33. A. Melloni, R. Costa, G. Cusmai, and F. Morichetti, "The role of index contrast in dielectric optical waveguides," Int. J. Mater. Prod. Technol. **34**(4), 421–437 (2009).
34. I.-C. Khoo, *Liquid Crystals* (John Wiley & Sons, 2007), pp. 1–190.
35. A. G. Maksimochkin, S. V. Pasechnik, G. I. Maksimochkin, and V. G. Chigrinov, "Electrically controlled waveguide mode in LC layer for fiber optic applications," Opt. Commun. **283**(16), 3136–3141 (2010).
36. A. K. Pitilakis, D. C. Zografopoulos, and E. E. Kriezis, "In-line polarization controller based on liquid-crystal photonic crystal fibers," J. Lightwave Technol. **29**(17), 2560–2569 (2011).
37. D. C. Zografopoulos and R. Beccherelli, "Design of a vertically coupled liquid-crystal long-range plasmonic optical switch," Appl. Phys. Lett. **102**(10), 101103 (2013).
38. D. Dai and J. E. Bowers, "Novel concept for ultracompact polarization splitter-rotator based on silicon nanowires," Opt. Express **19**(11), 10940–10949 (2011).
39. Q. Wang and S. Kumar, "Submillisecond switching of nematic liquid crystal in cells fabricated by anisotropic phase-separation of liquid crystal and polymer mixture," Appl. Phys. Lett. **86**(7), 071119 (2005).
40. J. P. Barber, D. B. Conkey, M. M. Smith, J. R. Lee, B. A. Peeni, Z. A. George, A. R. Hawkins, D. Yin, and H. Schmidt, "Hollow waveguides on planar substrates with selectable geometry cores," in Conference on Lasers and Electro-Optics/Quantum Electronics and Laser Science and Photonic Applications Systems Technologies, Technical Digest (CD) (Optical Society of America, 2005), paper CTuD4.
41. Z. Zhang, Z. You, and D. Chu, "Fundamentals of phase-only liquid crystal on silicon (LCOS) devices," Light Sci. Appl. **3**(10), 1–10 (2014).
42. X. Chen and H. K. Tsang, "Polarization-independent grating couplers for silicon-on-insulator nanophotonic waveguides," Opt. Lett. **36**(6), 796–798 (2011).
43. P. Xu, Y. Zhang, Z. Shao, L. Liu, L. Zhou, C. Yang, Y. Chen, and S. Yu, "High-efficiency wideband SiNx-on-SOI grating coupler with low fabrication complexity," Opt. Lett. **42**(17), 3391–3394 (2017).

Optics EXPRESS

44. C.-C. Chiu and D.-W. Huang, "Polarization independent grating coupler for silicon-on-insulator waveguides," in 2010 International Conference on Optical MEMS and Nanophotonics (OPT MEMS), 2010, 171–172.
45. W. Bogaerts, D. Taillaert, P. Dumon, D. Van Thourhout, R. Baets, and E. Pluk, "A polarization-diversity wavelength duplexer circuit in silicon-on-insulator photonic wires," Opt. Express **15**(4), 1567–1578 (2007).
46. C. Alonso-Ramos, L. Zavargo-Peche, A. Ortega-Moñux, R. Halir, I. Molina-Fernández, and P. Cheben, "Polarization-independent grating coupler for micrometric silicon rib waveguides," Opt. Lett. **37**(17), 3663–3665 (2012).
47. V. Passaro and G. Masanovic, "Design of SiON-based grating-assisted vertical directional couplers," Opt. Express **14**(3), 1055–1063 (2006).
48. Y. J. Liu, P. X. Gao, B. Wong, and S. Keshav, "Quartz: a new design element for low-latency DCNs," in Proceedings of the 2014 ACM conference on SIGCOMM, Chicago, 2014, 283–294.
49. S. Aleksic, "The future of optical interconnects for data centers: a review of technology trends," in Telecommunications (ConTEL), 2017 14th International Conference on, Zagreb, 2017, 41–46.

1. Introduction

Optical cross-connect (OXC) switch is one of the most important components in the optical networks for telecommunication [1] and data centers [2–4], which alleviates the bandwidth bottleneck [1] by avoiding conventional optical-electronic-optical (OEO) conversion.

Various OXC techniques have been proposed and developed, with most remarkably and prevalently the free-space devices based on micro-electro-mechanical systems (MEMS) [5]. On-chip (planar) OXCs, which feature high compactness and easy integration, are also under intensive study [6]. Some typical examples are those based on Mach-Zehnder interferometer (MZI) optical switches [7], micro-ring resonators [8], semiconductor optical amplifier (SOA) based optical switches [9], MEMS silicon photonic switches [10–12], and so on. The firstly demonstrated MEMS silicon photonic switch [10] supports monolithic integration with 50 × 50 ports, and realizes sub-microsecond optical circuit switching (OCS) with around 28 dB maximum optical insertion loss. The more recent device using vertical adiabatic couplers presents remarkable on-chip insertion loss down to 3.7 dB (coupling loss of 12 dB) for 64 × 64-port switching [11]. As for nematic liquid crystal (NLC), the planar OXC was reported using tunable total-internal reflection (TIR) interfaces in the NLC trenches [1]. However, the requirement of high surface quality in the trench and the limited refractive index (RI) contrast pose critical limitations to practical TIR NLC OXCs. The OXCs with superior overall performances are still under exploration, in the aspects including scalability, switching speed, optical loss, power consumption, robustness, durability and so on [6].

In this paper, a planar OXC solution is proposed based on polarization-dependent (PD) routing in NLC (P-OXC for short). The P-OXC consists of a square array of unit cells in the standard cross-bar fabric [1]. In each unit cell, the input polarized light first goes through an electrically controllable polarization rotator to maintain/rotate the light polarization, which is realized by the electrically-driven NLC reorientation in the NLC waveguides. It mimics the free-space polarization rotator using twisted NLC with crossing alignment (so called twisted nematic effect) [13–15], which is different from the other waveguide-based mode converters [16–18]. Then the light enters a PD waveguide unit with the cores using the pre-aligned NLC and the RI-matched material, in which the light path is determined by the light polarization state. The combination of both enables the switching of input light to one of the two output ports, corresponding to either the lead-in/lead-out state or the bending state. The unit cells work together to form a non-blocking, planar, polarization-routed OXC system.

The proposed scheme of P-OXC is first illustrated in Section 2, and the device design is then depicted in Section 3. The analysis and simulation of the device are presented in Section 4, followed by the discussions on practical issues in Section 5.

2. Proposed scheme

The scheme of P-OXC is sketched in Fig. 1(a), using a 4 × 4 design as the example for easy illustration. The light beams are injected into the input ports (I_1, I_2, …, I_N in Fig. 1(a)) on the left side, and they are then switched and delivered separately to the output ports (O_1, O_2, …,

Optics EXPRESS

O_N in Fig. 1(a)) located on the bottom side. In each unit cell, it either conveys the light beams forward, or turns them into the perpendicular direction (see Fig. 1(c)).

As shown in Fig. 1(b), the unit cell consists of a five-layered structure. The waveguide layer in the middle (yellow color) has the NLC filled into the chamber to form the waveguide cores, sandwiched by two cladding layers (blue color) with alignment layers (light red color) coated inside. The bottom cladding layers are patterned with CMOS circuits for electrical driving, which is not explicitly shown here. The waveguide layer is patterned with polymer cladding structure, metal electrodes and also the RI-matched bending core.

More details of the waveguide layer are sketched in Fig. 1(c). The waveguide crossing is connected by two polarization rotators at the input port of lead-in waveguide and the output port of lead-out waveguide, respectively. The waveguide tapers are applied to compress the mode in the polarization rotators and to expand it at the crossing, in order to reduce both the driving voltage and the crossing loss. The RI-matched core utilizes the material that has polarization-independent but nearly the same RI as the extraordinary RI of NLC.

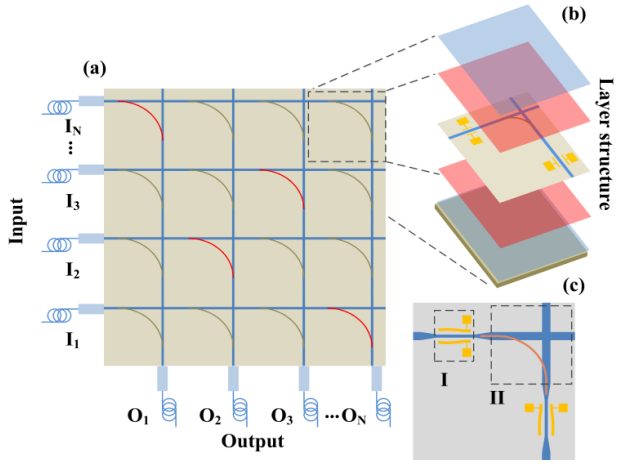

Fig. 1. (a) The P-OXC is sketched, with the five-layered structure of the unit cell shown in (b). The pattern of the NLC layer in the unit cell is shown in (c). Part I and Part II in (c) represent the polarization rotator and the PD waveguides, respectively.

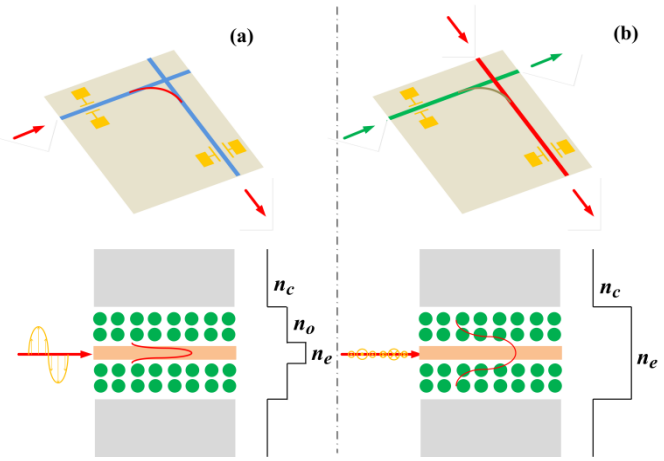

Fig. 2. The working principle of polarization-dependent routing in a single unit cell, including (a) the bending state and (b) the lead-in/lead-out state. The upper rows illustrate the paths of the light in each state, while the lower ones present the mechanisms of polarization-dependent waveguides. In the lower subfigures, the green dots stand for the NLC, the pink part for RI-matching core, and the grey ones for the outer claddings.

Optics EXPRESS

The working states of a single unit cell are illustrated in Fig. 2. If the incoming light is at the transverse electric (TE) mode, the RI-matched core has the RI of n_e, while the NLC has a lower RI of n_o (ordinary RI). In this regard, the light is confined in the narrow RI-matched core and propagates along the bending (see Fig. 2(a)). This is called the bending state. In contrast, when the incoming light is at the transverse magnetic (TM) mode, it experiences the same RI of n_e in both the RI-matched core and the NLC. In this way, a broad straight waveguide is formed using the RI-matched part and the NLC as the core and the outer part (the RI $n_c < n_e$) as the cladding. The light thus propagates along the straight path as shown in Fig. 2(b), corresponding to the lead-in/lead-out state. With these, the propagation direction is purely dependent on the polarization state of input light. Thus, a passive switching is realized.

Another key component in the P-OXC is the in-plane polarization rotator (see I in Fig. 1(c)), which is electrically controllable to convert the light polarization between the TE and the TM modes. As shown in Fig. 3, the mechanism of polarization rotation is to pre-align vertically the NLC in the waveguide, and to then apply the gradient electric field to drag the NLC gradually to the planar direction along the waveguide. It mimics the polarization rotator in free space, which directly uses the twisted NLC that has the helical direction along the LC cell thickness. When the Mauguin condition [15] is met, the polarization rotation is achieved as explained in Section 4.

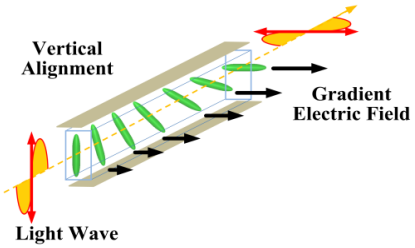

Fig. 3. The mechanism of the in-plane polarization rotator.

3. Device design

This section will elaborate the device design and the material choices, covering mainly the layered structure, the PD waveguides and also the polarization rotator.

Table 1. Main properties of the materials in the sample device

Material	Permittivity (1 kHz)	Refractive Index	Optical Loss
5CB	7 (⊥), 18 (//) [25]	Ref [26]. (n_e: 1.682, n_o: 1.520 @1550 nm)	2 dB/cm @1550 nm [27, 28]
Al	—	Ref [29]. (1.44 - **i**16 @1550 nm)	—
SiO_2	3.91 [31]	Ref [29]. (1.444 @1550 nm)	—
NOA84	~4* [30]	1.46 [22]	~1 dB/cm* @1550 nm [22]
RI-core	~12.5** [23]	1.68 [23, 24]	0.5 dB/cm** @1310 nm [23, 24]

*Estimated for NOA84; **Estimated for the RI-core.

3.1 Layered structure

As aforementioned, there are mainly five layers in the proposed device (see Fig. 1(b)). The cladding layers (blue color in Fig. 1(b)) are thin films of SiO_2 for the light confinement in the vertical direction. As for the bottom cladding layer, the SiO_2 thin film is deposited on the substrate with pre-fabricated CMOS circuit. The top cladding layer can use simply quartz or SiO_2 thin film on silicon wafer. The alignment layers (light red color in Fig. 1(b)) are deposited inside the cladding layers and provide vertical (homeotropic) alignment for the NLC. Several materials have been used for the vertical alignment, including polyimide [19], polydimethylsiloxane (PDMS) [20], liquid crystalline polymer (LCP) [21], etc. The LCP thin

Optics EXPRESS

film with the thickness of 5 nm is adopted in our sample device, which can be fabricated using the method similar to [21].The waveguide layer (yellow color in Fig. 1(b)) is the most important functioning layer and is chosen to have the thickness of 1 μm. It is patterned to have the polymer cladding structure, the metal electrodes and also the RI-matched bending core (RI-core for short, see Fig. 2) using the materials of NOA84 [22], aluminum and polymer [23] (or SiON [24]), respectively. The NLC in the design is 5CB [13]. The main material properties [22–31] are listed in Table 1. The RI models of 5CB is the extended Cauchy equations [26]. The RI models of aluminum and SiO_2 in finite-difference time-domain (FDTD) simulations are from Palik [29]. In the NLC orientation calculation, the elastic constants are K_{11} = 6.4 pN, K_{22} = 3 pN, K_{33} = 10 pN [13].

3.2 Polarization-dependent waveguides

The design of the PD waveguides is sketched in Fig. 4(a). The main parts of the PD waveguides are the waveguide crossing with the NLC-core (blue color), and the waveguide bending with the RI-core (red color). The polymer NOA84 (gray color), which has nearly the same but slightly higher RI as SiO_2, is applied as the waveguide cladding. Waveguide tapers [32] are used between the polarization rotators and the PD waveguides for mode compression/expansion.

The width of the RI-core is 2 μm, and the width of the NLC-core is 8 μm. The radius of the waveguide bending is 50 μm, which has relatively low bending loss according to the thumb of rules [33]. The waveguide crossings are 90-degree crossing, which largely suppress the crossing loss and the cross-talk [7, 10]. In addition, two crossings are implemented at the crossing points of the RI-core bendings and the NLC-core waveguides. These two crossings help suppress the losses at these points with the 90-degree crossing condition.

It is noted that the NLC is pre-aligned vertically as aforementioned. In order to keep the LC at the nematic phase, it is essential to control the working temperature of the device at about 25 °C [13, 34]. The issue of RI mismatching between the RI-core and the NLC will be studied in Section 4.

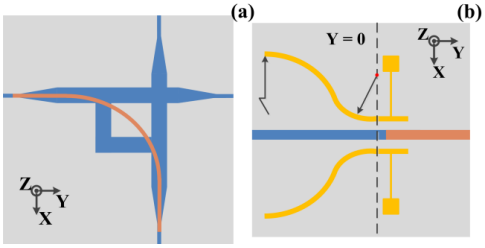

Fig. 4. (a) The pattern of the polarization-dependent waveguides. The blue portion stands for the NLC, the red one for the RI-core, and the gray one for the NOA84 outer cladding part. (b) The pattern of the polarization rotator. The blue portion stands for the NLC, the red for RI-core, the golden for Al and the gray for NOA84.

3.3 Polarization rotator in a NLC-core waveguide

The design of the polarization rotator in NLC-core waveguide is illustrated in Fig. 4(b). For succinct illustration, the coordinate O-XYZ is applied. The position Y = 0 μm is defined at the dash line according to the center of the arc in Fig. 4(b).

The main structure of the polarization rotator is a NLC-core waveguide with the symmetric electrodes on its both sides. At the output end of the polarization rotator, the RI-core waveguide is connected directly to the NLC-core waveguide. For low-loss coupling, the NLC-core waveguide and the RI-core waveguide has the same width of 2 μm. Each electrode consists of a straight portion and two arcs, which are tangential to each other at the junction. The straight portion is designed to cover both the NLC-core and RI-core waveguide in length, which should be short enough to reduce the absorption loss. The bending angle of the two

Optics EXPRESS

arcs is 0.472 rad. The radius of the arc adjacent to the straight waveguide is 11 μm, while the radius of the other arc is 99 μm. The width of the electrode is 2 μm. The coplanar electrodes are connected through vias to the CMOS circuit on the substrate (not shown in Fig. 4(b)).

To reduce the absorption of metal electrodes, the gap between the straight portions of two electrodes should be large enough. Here it is designed to be 4 μm. The gap is determined by the pre-calculation of the optical mode field in the NLC-core waveguide, whose width is below 4 μm with 99% power-in-the-bucket over the O band, the C band and the L band.

The curvy shape of electrodes enables to generate a gradually varying spacing and thus a non-uniform electric field. The driving voltage is an AC sinusoidal wave of 35V and the frequency of 1 kHz, which can avoid the electrolyze effect and the possible electro-hydrodynamics (EHD) instabilities [35]. The driving electrode can be switched on and off between 35 V AC and 0 V. The protrusion of the RI-core waveguide into the NLC waveguide provides a stop for the NLC under electric field, and also minimizes the RI mismatching between the RI-core and the NLC for the TE mode.

4. Simulations

With the above sample device, simulations and analyses will be carried out to estimate and optimize the performance.

4.1 Theory and method

The NLC is commonly modeled as the composite of rod-like molecule in physics, and the NLC of 5CB is uniaxial [13, 34]. The orientation of the molecule director can be defined by the tilt angle θ and the twist angle φ in the cylindrical coordinate, as shown in Fig. 5.

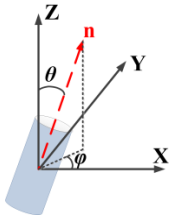

Fig. 5. Definition of the orientation of the LC molecule's director using the tilt angle θ and the twist angle φ.

Then, the director **n** can be thus written as

$$\mathbf{n} = \sin(\theta)\cos(\phi)\hat{\mathbf{X}} + \sin(\theta)\sin(\phi)\hat{\mathbf{Y}} + \cos(\theta)\hat{\mathbf{Z}}. \quad (1)$$

In the NLC, the LC orientation configuration is pre-determined by the surface alignment. Under an external electric field, a local torque is exerted on the LC molecule and rotates the director, which in turn affects the local electric field. Based on the Oseen-Frank continuum elastic theory [13, 34, 36], the existing configuration of the LC orientation satisfies the minimization of total free energy F_{tot}, which is defined as the volume integral of free energy density F_d , as given by,

$$F_{tot} = \iiint_V f_d dV = \iiint_V f_{ela} + f_E dV, \quad (2)$$

where f_d composes of two terms in the presence of external electric field, namely the elastic free energy f_{ela} and the electric-field free energy f_E.

The elastic free energy density depicts the local elastic deformation of the NLC as follows,

$$f_{ela} = \frac{1}{2}K_{11}(\nabla\cdot\mathbf{n})^2 + \frac{1}{2}K_{22}(\mathbf{n}\cdot\nabla\times\mathbf{n})^2 + \frac{1}{2}K_{33}(\mathbf{n}\times\nabla\times\mathbf{n})^2, \quad (3)$$

Optics EXPRESS

in which K_{11}, K_{22}, and K_{33} denote the components of elastic constant, and the three terms correspond to the three possible deformations of LC, namely splay, twist and bend, respectively.

Regarding the electric-field free energy density, it describes the rotation of LC by the locally applied electric force and can be formulated as

$$f_E = \frac{1}{2}\mathbf{E}\cdot\mathbf{D} = -\frac{1}{2}\varepsilon_0\left[\varepsilon_\perp\mathbf{E} + \Delta\varepsilon\left(\mathbf{E}\cdot\mathbf{n}\right)\mathbf{n}\right]\cdot E = -\frac{1}{2}\varepsilon_0\varepsilon_\perp E^2 - \frac{1}{2}\varepsilon_0\Delta\varepsilon\left(\mathbf{E}\cdot\mathbf{n}\right)^2, \quad (4)$$

in which **E** is the electric field and **D** is the electric displacement. The formulation can be further expanded by applying the relation **D** = ε**E** with the local permittivity ε as expressed by the diagonal tensor

$$\varepsilon = \begin{bmatrix} \varepsilon_\perp & & \\ & \varepsilon_\perp & \\ & & \varepsilon_{//} \end{bmatrix}. \quad (5)$$

The resulted formulation then consists of two terms – a director-independent term and a director-dependent term with the dielectric anisotropy $\Delta\varepsilon = \varepsilon_{//} - \varepsilon_\perp$ [13]. As for the NLC used in the P-OXC, the dielectric anisotropy is positive, and the LC director tends to be parallel with the local electric field.

The local LC director rotation under a non-uniform electric field distribution is complicated when the local permittivity of the NLC takes into account both low frequency and optical frequency [36]. The local permittivity of the LC is defined as

$$\varepsilon = \begin{bmatrix} \varepsilon_\perp + \Delta\varepsilon n_x n_x & \Delta\varepsilon n_y n_x & \Delta\varepsilon n_z n_x \\ \Delta\varepsilon n_x n_y & \varepsilon_\perp + \Delta\varepsilon n_y n_y & \Delta\varepsilon n_z n_y \\ \Delta\varepsilon n_x n_z & \Delta\varepsilon n_y n_z & \varepsilon_\perp + \Delta\varepsilon n_z n_z \end{bmatrix}, \quad (6)$$

in which **n** = (n_x, n_y, n_z).

The configuration of the NLC is calculated by minimizing the aforementioned total free energy using the weak-form partial differential equation (PDE) solver in COMSOL. The strong anchoring boundary condition [36, 37] is applied, with θ = 0 and φ = 0 at the interface between LC and alignment layer.

Besides the free-energy minimization, it is essential to consider the coupling between the electric field and the LC director configuration [37]. To resolve the coupling problem, an iteration scheme is applied for the complicated 3D models. It calculates in sequence the electric field with the current LC director configuration, and then the next LC director configuration with the average between the previous and current electric field. The iteration stops when the RMS (root mean square) error between the previous and the current electric field reaches 0.0001 of the driving voltage. The low-frequency (1 kHz) local permittivity defined in Eq. (6) is used for the calculation of electric field with the aforementioned coupling issue. The optical field propagation in the proposed device is simulated using FDTD (Lumerical FDTD Solution). In the FDTD, the Liquid Crystal group is applied to model the permittivity distribution of LC.

4.2 Polarization rotator in a NLC-core waveguide

As shown in Fig. 4(b), the polarization rotator has the structure of mainly a straight NLC-core waveguide with coplanar electrodes on its both sides. A RI-core waveguide is protruded into the output end of the NLC-core waveguide as mentioned above. To complete the design, it is important to further determine the optimal position of the junction and also the sensitivity of the conversion loss to the position deviation due to the fabrication limit.

Optics EXPRESS

To calculate the optimal junction position and the sensitivity, a simplified structure is first modeled, where no RI-core waveguide but an infinitely-long NLC-core waveguide and straight electrodes are applied. The optimal position is then chosen according to the minimum conversion loss, and the structure is finally determined and simulated with the optimal junction position.

The NLC orientation distribution is calculated using the tilt angle θ and the twist angle φ defined in Fig. 5. At the waveguide center, the distribution of the tilt angle θ along the propagation direction is presented in Fig. 6(a). It can be seen that in the ideal case, the tilt angle varies linearly along the propagation direction, while the distribution deviates from the baseline in the designed polarization rotator (either without RI-core waveguide, or with the RI-core waveguide at the optimal junction position). In the designed polarization rotator, the θ distribution across the cross-section (at Y = 0 μm) is also presented in Fig. 6(b). It can be seen that the hard-anchoring condition at the boundaries forces the director orientation to change gradually across the thickness and the width, which is different from the perfect uniform one in the ideal case.

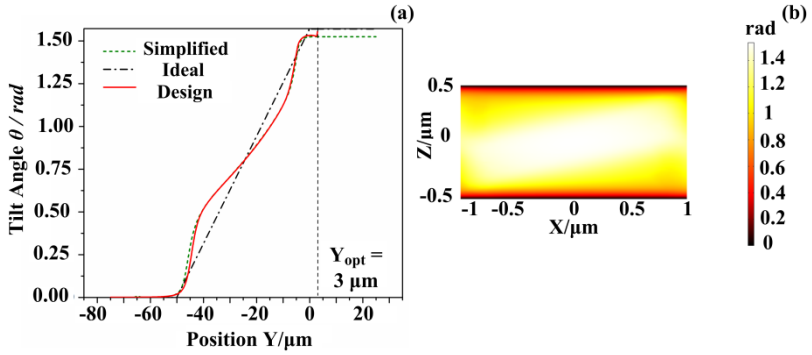

Fig. 6. (a) Distributions of the tilt angle θ along the waveguide center in the ideal case, the simplified model, and the sample device. (b) The θ distribution across the cross-section at the position Y = 0 μm in the sample device.

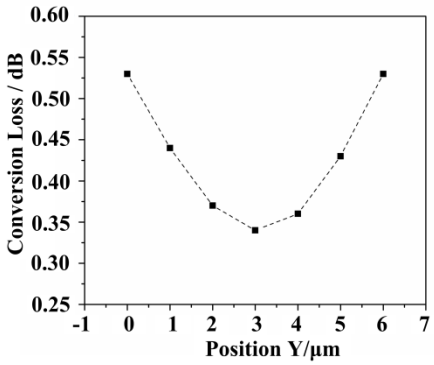

Fig. 7. Conversion losses at different cross-sections.

As for the twist angle φ, it is zero for the ideal case and around ± 0.18 rad at maximum for the other two cases. It is noted that a smaller dielectric constant of the RI-core material would lead to the increase of the twist angle at the corner of the junction (up to ± 0.4 rad for 35 V @1 kHz), but the effect on the light propagation can be neglected, which is not shown in the following discussion.

In the operation of the bending state, the light polarization is firstly converted from the TM mode to the TE mode by the polarization rotator at the input end, and then it is rotated back to the TM mode again at the output end. For simplification, only the TM-to-TE mode

Optics EXPRESS

conversion is considered when the simplified model is simulated to determine the optimal junction position Y_{opt}. With these, the conversion losses at different cross-sections are calculated and plotted in Fig. 7. It can be seen that the optimal junction position is Y = 3 μm, with the conversion loss as around 0.34 dB. The increase of conversion loss is below 0.19 dB when the cross-section deviates from the Y_{opt} within the range of ± 3 μm.

Both the performances in the TM-to-TE and the TE-to-TM conversion are simulated for the sample device at the central wavelength of the O band (i.e., 1310 nm). For comparison, the conversions in the two directions are also calculated for the ideal case.

In Fig. 8, the light propagation along the designed polarization rotator is presented for the TM-to-TE conversion. The cut plane for observation is perpendicular to Z direction and locates at the center of the waveguide layer. It can be seen that the input TM mode (Z-polarization) is almost fully converted into the TE mode (X-polarization) by the rotator.

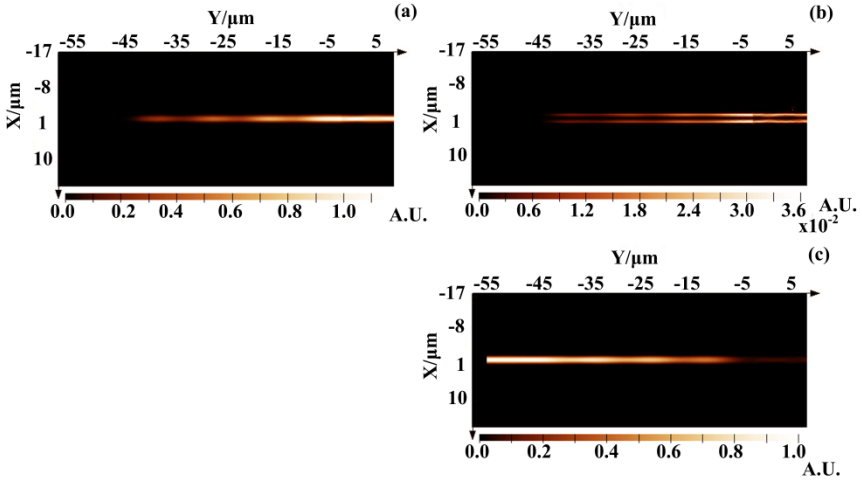

Fig. 8. Simulated propagation light field of the sample device in the TM-to-TE conversion, with (a) X-, (b) Y-, and (c) Z-polarization components. The cut plane for observation is perpendicular to the Z direction and locates at the center of the waveguide layer.

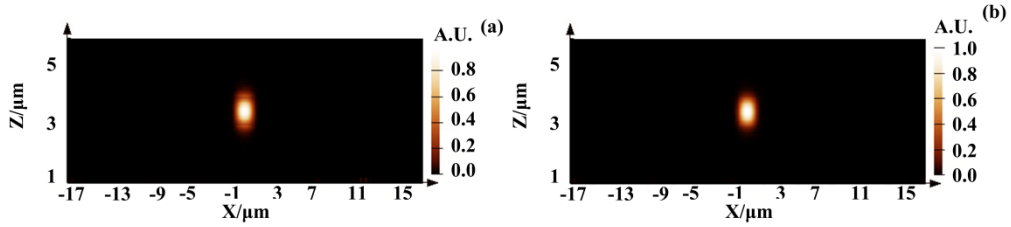

Fig. 9. The cross-sectional mode fields near (a) the input at Y = –54 μm and (b) the output at Y = 6 μm, respectively. For the input, the Z-polarization component is shown, while for the output, the X-polarization component is presented.

In Fig. 9, the cross-sectional mode fields are presented for the position near the input end (Y = –54 μm) and the output end (Y = 6 μm), respectively. Figure 9(a) shows the Z-polarization component on the input side, while Fig. 9(b) shows the X-polarization component on the output side. It can be seen that the field patterns are almost the same in both sub-figures, proving the successful rotation from the Z-polarization (i.e., the TM mode) to the X-polarization (i.e., the TE mode).

The calculated conversion losses in the TM-to-TE conversion are 0.49 dB and 0.20 dB while those in the TE-to-TM conversion are 0.54 dB and 0.20 dB, for the sample device and the ideal case, respectively. The conversion losses for different bands (the C band and the L

Optics EXPRESS

band) are also calculated for both the designed polarization rotator and the ideal case. For simplification, only the central wavelengths of the bands are considered, and only the TM-to-TE conversion is simulated. The results are summarized in Table 2. It can be seen that the polarization rotator works well over the broad bandwidth covering the O band, the C band and the L band, which is similar to the ideal case. Due to long helical pitch of the NLC, the rotation of polarization direction is broadband.

Table 2. TM-to-TE conversion losses @ different wavelengths

Wavelength	Conversion loss for designed device	Conversion loss for ideal case
1310 nm	0.49 dB	0.20 dB
1548 nm	0.72 dB	0.27 dB
1595 nm	0.48 dB	0.29 dB

Further simulations are carried out to investigate the dispersion of conversion loss over the O band, and the result is presented in Fig. 10. When no driving voltage is applied, the polarization rotator is simply an NLC-core waveguide under the vertical alignment. Thanks to the sufficient spacing of the electrodes, the absorption loss is alleviated. The propagation losses for the zero-voltage case are also calculated, which are about 0.048 dB for the three considered bands.

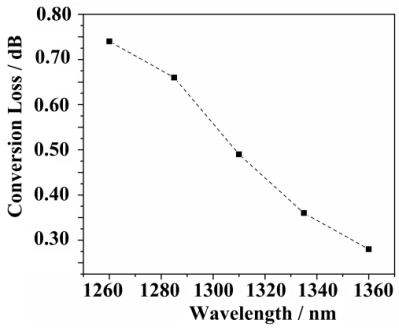

Fig. 10. Dispersion of the conversion loss over the O band in the TM-to-TE conversion.

As shown in Table 2 and Fig. 10, the conversion loss is dependent on wavelength. In the ideal case, the electrode absorption is increased at longer wavelength, because of the normal dispersion in NLC and the wider mode field from diffraction limit. As for the designed device, the reasons can be two-fold. Besides the aforementioned factor in the ideal case, the deviation from ideal linear NLC distribution results in the mismatch of polarization rotation and NLC tilt angle. There is post-rotation or early-rotation for some wavelength through the waveguide, and a wider mode field occurs at the region where RI is below n_e (particularly near the output end). Thus, the conversion suffers from additional wavelength-dependent loss.

4.3 Polarization-dependent waveguides

The PD waveguide is the other key element in the proposed design, which can passively select the light path according to the light polarization. From the sample device in Fig. 4, the waveguides consist of the NLC-core waveguides and the RI-core ones. The RI of RI-core material is tuned to match the extraordinary RI of NLC, and it is important to determine the impact of RI mismatching. It is noted that the waveguide tapers are not included in the simulations for simplifications, and the propagation loss of waveguide tapers can be suppressed by proper structural design and parameters [32]. For simplification, only the performance at 1310 nm is evaluated for the sample device. The simulations are carried out in the perfectly-matched RI case, for the lead-in, the lead-out and the bending operations

Optics EXPRESS

Based on the 3D simulation, the light propagation fields (amplitude) are presented in Fig. 11 for the three operations. Similarly, the cut plane for observation is perpendicular to the Z direction and locates at the center of the waveguide layer. In Fig. 11, the calculated propagation losses are 0.03 dB, 0.02 dB, and 0.07 dB for the three operations of bending, lead-in, and lead-out, respectively. Similarly, the cross-talk can be determined for each of the three operations. From the 3D simulations above, the cross-talk for the three processes are about −43 dB, −27 dB and −53 dB, respectively.

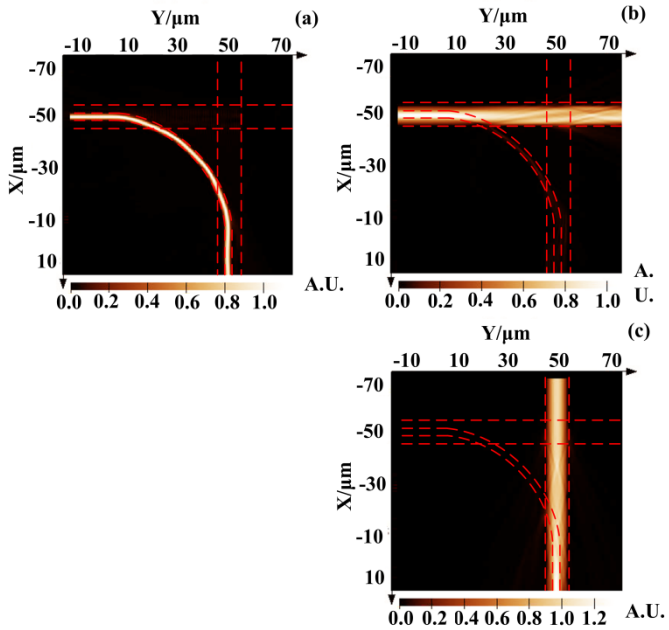

Fig. 11. Simulated propagation light fields (amplitude) in the perfectly-matched RI case, for the operations of (a) bending, (b) lead-in, and (c) lead-out. The cut plane for observation is perpendicular to the Z direction and locates at the center of the waveguide layer.

Table 3. Propagation losses with different RIs of RI-core @ 1310 nm

RI of RI-core	Propagation loss for lead-in	Propagation loss for lead-out	Propagation loss for bending
1.680	0.07 dB	0.04 dB	0.07 dB
1.682	0.05 dB	0.04 dB	~0
1.684	0.03 dB	0.04 dB	~0
n_e (1.683)	0.03 dB	0.04 dB	~0

For the RI-mismatching cases, the simulations are performed in 2D, which is more computationally efficient. The propagation losses with different RIs of the RI-core are listed in Table 3. It can be seen that the worst performance degradation occurs when the RIs of RI-core is 1.680. The maximum increase of the propagation losses is around 0.07 dB, as compared to the case with the perfectly-matched RI (when RI of RI-core is n_e). However, it is more favorable to keep the RI-core's RI at the value of no more than n_e, so that the cross-talk can be specially suppressed for the lead-in process. It is noted that there is a slight difference between the propagation losses in the lead-in and the lead-out processes. It is mainly due to the asymmetric facets of the bending portion (RI-core). Since the outer-edge is less abrupt, the propagation loss is less sensitive to the RI difference of RI-core in the lead-out process.

Optics EXPRESS

5. Discussions

With design and simulations above, other practical issues will be further discussed, including the loss scaling, the switching speed, the device fabrication and the fiber-to-chip coupling.

5.1 Insertion loss and cross-talk

Considering the conversion loss and the propagation loss characterized in the simulations, the total insertion loss for the proposed device with $N \times N$ unit cells can be determined, with the scaling equation as follows,

$$\begin{aligned} T = &(T_{TM-TM} + L_R T_{LC} + T_I + L_I \beta T_{LC}) \times (N\text{-}1) \\ &+ (T_{TM-TE} + T_{TE-TM} + 2L_R T_{LC} + T_B + L_B T_{SiON}) \\ &+ (T_{TM-TM} + L_R T_{LC} + T_O + L_O \beta T_{LC}) \times (N\text{-}1) + T_C, \end{aligned} \tag{7}$$

in which $T_{TM\text{-}TM}$, $T_{TM\text{-}TE}$, $T_{TE\text{-}TM}$ denote the propagation losses in the corresponding polarization conversions. The subscripts of R, I, O, and B stand for the polarization rotator, the operations of lead-in, lead-out and bending, respectively. The material losses of the NLC and the RI-core (SiON), which includes the absorption loss and the scattering loss in the lump, are T_{LC} and T_{SiON}, respectively. The coefficient β is set as 1.5 to equivalize the volumes of the NLC and the RI-core in the polarization-dependent waveguides. The term T_c refers to the coupling loss at the input/output port and is set as 3 dB.

For demonstration, the O-band is considered in the calculation of the total insertion loss. The material losses can be referred to Table 1. In the sample device, the length of polarization rotator L_R is about 70 μm, and the lengths of lead-in/lead-out waveguides, namely L_I and L_O, are the same as 180 μm (including the tapers). In the bending operation, the propagation length L_B consists of part of the lead-in/lead-out waveguides and also a quarter of the circle. The length L_B is approximately 140 μm in the sample device.

Using Eq. (7) and the above data, the total insertion loss T for different numbers of input/output ports N can be evaluated, which is plotted in Fig. 12. For a small 8 × 8 OXC device, the maximum on-chip insertion loss is estimated to be about 3 dB, and the maximum path dependent loss is around 2 dB. If the port number becomes 32 × 32, the total insertion loss is increased to ~14 dB. Although the loss and the cross-talk in the polarization rotator are varied when the polarization conversion is performed, they are largely suppressed since only one unit cell works in the bending state for each route.

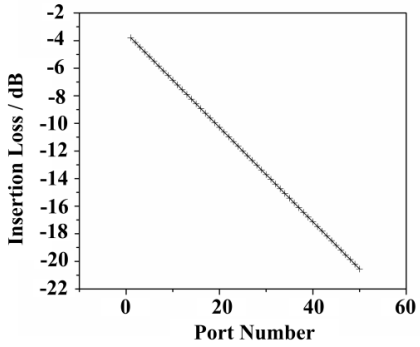

Fig. 12. Total insertion loss for different port numbers at the wavelength of 1310 nm.

With the cross-talks in the unit cell (Section 4.3), the signal-to-cross-talk ratio SXR [1] can be estimated as $-X_I - 10\log_{10}(N-1)$, and $-X_B - X_I - 10\log_{10}(N-1)$, for the worst case ($I_N$ to O_1) and the best case (I_1 to O_N). Here X is the cross-talk in each unit cell. For the 8 × 8

Optics EXPRESS

OXC, an average cross-talk is achieved down to −40 dB. The worst and the best cross-talks in 8 × 8 OXC are estimated to be −19 dB and −62 dB, respectively.

Some modifications can be implemented to further enhance the loss performance. By using the strategies in [10] and [11], more efforts should be made to suppress the propagation loss in the lead-in/out processes. The PD waveguide can be replaced by an on-chip polarization beam splitter (PBS) using SiON or silicon material [38], and the waveguide crossing can be upgraded using the low-loss designs [10, 11]. With the lower loss in the PBS (e.g. 0.017 dB [38]), waveguide crossing (e.g. 0.01 dB [10, 11]) and the solid-material waveguide (e.g. SiON with 0.05 dB/mm [23, 24]), the 32 × 32 OXC is estimated to have maximum on-chip insertion loss of 5.1 dB and average crosstalk of −50 dB.

5.2 Switching speed

In the sample device, the waveguide layer is as thin as 1 μm, and a thinner layer can be used at the cost of an increased driving voltage. Considering the thin waveguide layer of the sample device, the switching time (including both on and off) can be about 1 ms [39]. Using a larger driving voltage of 50 V and a thinner layer, a switching time down to sub-milliseconds is possible. Instead of the pre-alignment layers, it is also potential to apply an additional top-bottom electrode pairs for the NLC alignment in the vertical direction. The turn-off time and the driving voltage are expected to be further reduced. These structures are feasible with the existing fabrication techniques, such as the hollow liquid-core waveguide on silicon [40].

5.3 Device fabrication

As for the sample device, it can leverage on the LCD/LCoS fabrication technology [41]. However, the patterning for polarization rotator and PD waveguides makes the fabrication tougher than the conventional LCD/LCoS devices. With better design, the alignment tolerance can be under control (e.g., see Fig. 7). For the thickness control of RI-core and NLC waveguide, the key point is the matching between RI-core and cladding. Some strategies can be developed to ease the fabrication, such as etching for the NLC core after the patterning of RI-core and cladding (NOA84 in the sample design). For the design using SiO_2 as the cladding, the more compatible techniques can be applied on silicon platform, e.g., surface polishing for thickness matching.

5.4 Fiber-to-chip coupling

Another important practical issue is the fiber-to-chip coupling. To achieve the polarization-dependent routing in the P-OXC, the coupled light wave to the access waveguide should be preprocessed to be in either the TM or the TE mode. The polarization-independent coupling is also preferred, since the polarization is dynamically randomly-rotating in the real optical communication systems. This issue is common in the silicon photonic and nano-photonic waveguides in photonic integrated circuit [38, 42]. Using the current techniques including the integrated polarization splitters, rotators and couplers [38, 42–47], several potential solutions can be found to address the polarization issue in P-OXC.

The elegant method of polarization diversity can be adopted [45] in our proposed device, as shown in Fig. 13. In principle, the diversity can be either space-based (see Fig. 13(a)) or mode-based (see Fig. 13(b)). For each port, the orthogonal polarization fields from (into) the fiber are pre-processed by the polarization splitter (combiner). One of the polarization fields is then rotated to its orthogonal counterpart. It is noted the polarization rotation can be performed simultaneously with the polarization splitting in the same structure. The on-chip polarization manipulation is with better compactness and integration than the fiber-based techniques, and is mainly adopted and discussed in P-OXC.

As for the space-based polarization diversity in Fig. 13(a), two copies of the P-OXC are placed side by side on the same chip. The polarization-independent grating coupler can be used as the fiber-to-chip interface. In the state of the art of grating couplers, the coupling

Optics EXPRESS

efficiency exceeds 50% and the available bandwidth covers the whole C-band [43]. The length of grating coupler is typically about a hundred μm [44]. The additional loss and footprint are thus acceptable in P-OXC with grating coupling.

Taking input port 1 (I_1) as an example, the input field from the fiber has dynamically random-rotating polarization. With the help of a compact fiber coupler grating using an integrated polarization splitter, both the fiber polarizations are coupled to TE-mode (or TM-mode) of their own waveguides. The light waves from both the waveguides are conveyed to the two copies of P-OXC at the corresponding input port pairs (e.g. I_1). They then ideally propagate through the same selected route, and experience the same attenuation and phase shift. Finally, they are coupled from the grating coupler at the output port pairs back into the output fiber. In principle, the grating couplers at the input and the output side are in the same form, and the output field polarizations can be perfectly restored to the input ones. In practical applications, the fabrication error should be controlled, and in this way the relative delay between the coupled light waves is expected to be precisely suppressed.

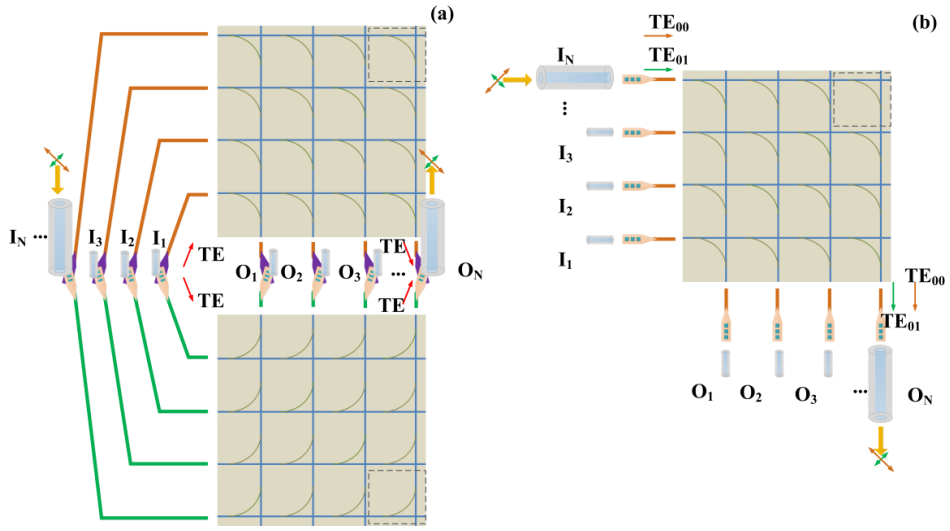

Fig. 13. The polarization diversity is used for fiber-chip coupling in P-OXC, including (a) the space-based and (b) the mode-based method. Only the case of TE mode is shown for example.

To apply the grating couplers, two more practical issues should be considered, including the compatibility between the grating couplers and the NLC waveguides, and the fabrication of both the grating coupler and the NLC waveguide in the same platform.

As for the compatibility issue, one of the most important parameter is the thickness. From some highly-efficient broadband design [43], it can be seen that the thickness of access waveguide is around 500 nm. The micrometric design is also demonstrated in [46], where the thickness of access waveguide is around 1 μm. The thickness of LC waveguide in our proposed design is 1 μm, and it is expected to be compatible with the grating couplers. In fact, the design space of LC waveguide thickness is sufficient to range from several hundred nm to about 1 μm, because there is no resonant structure in P-OXC. The parameter optimization can be carried out to match the grating coupler and the NLC waveguide.

The other issue, the integration of both the grating coupler and the P-OXC during fabrication, can also be properly addressed. The fabrication of P-OXC can leverage on the LCoS fabrication technique [41], which is compatible to the grating coupler fabrication on the silicon platform. The single-step fabrication is reported recently for highly efficient wide-band grating coupler on the silicon platform [43]. Economic fabrication tool such as i-line lithography and stepper can be applied [46]. The SiON-based fiber-to-chip coupler is also

Optics EXPRESS

studied [47]. In this regard, it is potential to use the existing techniques to integrate grating coupler to P-OXC on the same chip, with acceptable fabrication cost and process complexity.

As shown in Fig. 13(b), the mode-based polarization diversity method is adopted with end-coupling. The diversity is realized by using the integrated polarization converter [38] at the front of each input (output) port. The orthogonal polarization fields from the single-mode fiber are converted to different order modes with the same polarization (e.g. TE_{00} and TE_{01} mode, respectively) and propagate in the same selected (multimode) route. In practical, the modal dispersion induces relative delay between the orthogonal polarization fields at the output. Due to the short propagation length (~mm) in P-OXC, the resulted delay is largely suppressed to allow bit-rate of several hundred Gbps. The polarization-independent grating couplers to single access waveguide are also reported in the seminal papers [42], [46] and can be used as the fiber-to-chip interface in the mode-based diversity scheme.

6. Conclusions

In conclusion, P-OXC is proposed for the planar OXC solution, based on the PD routing using the NLC waveguides. Each unit cell works in either the bending state or the lead-in/lead-out state, dependent on the in-plane polarization rotation and the PD waveguide routing. In terms of the mechanism of polarization rotation, it enables the electrical control of the NLC alignment in the waveguide. The NLC is tuned to aligned in either the vertical or the twisted direction (along the waveguide axis), which mimics the free-space polarization rotator using the crossing-aligned twisted NLC.

A sample device is proposed for performance evaluation and optimization. The key elements, the polarization rotator in NLC-core waveguides and the PD waveguides, are designed and analyzed. With the RI-matching between the RI-core and the extraordinary RI of NLC, the PD waveguides are formed by defining the waveguide structure, which supports the lead-in, the lead-out or the bending light path. In the polarization rotator, the electrically-controllable polarization conversion is achieved using the gradient electric field generated by the bottle-shape coplanar electrodes under the driving voltage of 35 V. It is also potential to apply an additional top-bottom electrode pairs for the NLC alignment in the vertical direction, which can further reduce the driving voltage and the switching time. From simulations, it is estimated that the 8 × 8 P-OXC exhibits a maximum on-chip insertion loss of 3 dB, an average total cross-talk of −40 dB, a switching time of 1 ms and a footprint of 2 mm × 2 mm. The maximum path dependent loss is about 2 dB. It is also found that the dispersion of loss and cross-talk is mild over broad bandwidth. The P-OXC has the structure similar to the LCoS, and can leverage the mature LCD/LCoS fabrication technology.

The P-OXC combines the advantages of planar waveguide and LC device in compactness, broad bandwidth and low loss. As an on-chip device, it has compact footprint and possible integration with other planar lightwave circuit (PLC) devices. It also inherits some superior strengths from LCD/LCoS devices, including low power consumption (~mW/port), good reliability (resistance/recovery to humidity and thermal impact), low cost (based-on mature fabrication technology and without 3D structure or moving component). With the overall performances and advantages, it is promising for optical circuit switching in future communication networks, e.g. robust and green data centers [48, 49].

Funding

Research Grants Council (RGC) of Hong Kong (the General Research Fund including N_PolyU505/13, PolyU 152184/15E and PolyU 152127/17E); The Hong Kong Polytechnic University (G-YBPR, 4-BCAL, 1-ZE14, 1-ZE27 and 1-ZVGH); National Natural Science Foundation of China (no. 61377068 and 61361166004).

Optics EXPRESS

Acknowledgments

This work was supported by the Research Grants Council (RGC) of Hong Kong, the Hong Kong Polytechnic University and National Science Foundation of China.